Nanoscale

Crystal Structure of Au25(SePh)18 Nanocluster and Insights into the Electronic, Optical and Catalytic Properties

Journal:	*Nanoscale*
Manuscript ID:	NR-ART-08-2014-004631.R1
Article Type:	Paper
Date Submitted by the Author:	11-Sep-2014

Complete List of Authors:	Song, Yongbo; anhui university, Zhong, Juan; Xiangtan University, Yang, Sha; anhui university, Wang, Shuxin; Anhui university, Cao, Tiantian; Anhui University, Department of Chemistry Zhang, Jun; Anhui University, li, peng; Anhui University, Hu, Daqiao; Anhui university, Pei, Yong; Xiangtan University, Chemistry Zhu, Manzhou; Anhui university, Deartment of Chemistry

Nanoscale

RSCPublishing

ARTICLE

Crystal Structure of $Au_{25}(SePh)_{18}$ Nanocluster and Insights into the Electronic, Optical and Catalytic Properties

Cite this: DOI: 10.1039/x0xx00000x

Received 00th January 2012,
Accepted 00th January 2012

DOI: 10.1039/x0xx00000x

www.rsc.org/

Yongbo Song,[a] Juan Zhong,[b] Sha Yang,[a] Shuxin Wang,[a] Tiantian Cao,[a] Jun Zhang,[a] Peng Li,[a] Daqiao Hu,[a] Yong Pei,[b]* and Manzhou Zhu[a]*

The crystal structure of selenolate-capped $Au_{25}(SePh)_{18}^-$ nanocluster is unambiguously determined for the first time, which provides a solid basis for deep understanding of the structure-property relationships. The selenolate-capped Au_{25} cluster shows noticeable differences from the previously reported $Au_{25}(SCH_2CH_2Ph)_{18}^-$ counterpart, albeit both share the icosahedral Au_{13} core and semi-ring $Au_2(SeR)_3$ or $Au_2(SR)_3$ motifs. Distinct differences in the electronic structure, optical, catalytic and electrochemical properties are revealed by coupling experiment with density functional theory (TD-DFT) calculations. Overall, the successful determination of the $Au_{25}(SePh)_{18}^-$ structure removes the ambiguity about its structure, and comparison with the thiolated Au_{25} counterpart helps us further understand how the ligands affect the properties of the nanocluster.

1. Introduction

Research on atomically precise nanoclusters has emerged as a new frontier in nanoscience research.[1–13] The thiolate-protected gold nanoclusters, denoted as $Au_n(SR)_m$, have attracted great attention due to their excellent stability and unique catalysis and optical properties.[14,15] These ultrastable and atom-precise gold nanoclusters are very promising as building blocks in nanotechnology such as biomedicine,[16] chemical sensing,[17] bioassays,[18] and bio-labeling.[19]

Among the thiolate-capped gold nanoclusters, $Au_{25}(SR)_{18}^-$ is the first identified nanocluster[20] and has since then undergone intensive studies because of unique structure and properties. The structure of $Au_{25}(SR)_{18}^-$ was successfully solved in 2008, which is composed of an icosahedral Au_{13} core and six $Au_2(SR)_3$ semi-ring motifs.[21-23] Based on the crystal structure, experimental and theoretical works have revealed a variety of unique properties of $Au_{25}(SR)_{18}$ that are not observed in bulk gold or conventional gold nanoparticles. Such unique properties include discrete electron energies levels,[21] enhanced photoluminescence,[24,25] extraordinarly catalysis[26] and delocalized electron-imparted magnetism.[27,28] The $Au_{25}(SR)_{18}^-$ exhibits high stability; for example, the structure was preserved in the switch of charge state from -1 to +1.

Recently, we together with other researchers are motivated to pursue the selenolate-capped gold nanoclusters by replacing the thiolate (SR) ligands with selenolate (SeR).[29-35] In comparison to the S atom, the electronegativity and atomic radius of selenium (Se) are closer to those of gold; therefore, the Au−Se bond is more covalent and has a higher bond energy than Au−S, which may further increase the particle stability.[36] Negishi et al. first reported the direct synthesis of $Au_{25}(SeC_8H_{17})_{18}^-$ from gold salt precusor and ligand exchange synthesis of $Au_{38}(SeC_{12}H_{25})_{24}$ from $Au_{38}(SR)_{24}$.[29-31] We have prepared the selenophenolate-protected Au_{25} and Au_{18} clusters as well.[32,33] The results have found that selenolate-capped $Au_n(SeR)_m$ nanoclusters possess different optical properties from those of the $Au_n(SR)_m$ counterparts; for example, the thiolate-capped Au_{25} cluster shows absorption bands at 400, 450, 675 nm and a tail band above 780 nm, whereas $Au_{25}(SeR)_{18}$ shows a redshift in the absorption band(s). The recent works on the structural determination of $Au_{24}(SePh)_{20}$ and $Au_{24}(SCH_2Ph\text{-}^tBu)_{20}$ revealed largely different structures and optical properties between the thiolate and selenolate systems.[37] This raises a question on the $Au_{25}(SePh)_{18}$ system in comparison to the crystallographically characterized $Au_{25}(SCH_2CH_2Ph)_{18}$; unfortunately, very limited information is available except their identical size. The lack of the atomic structure of $Au_{25}(SePh)_{18}$ precludes deep understanding of the physicochemical properties of selenolate-capped gold clusters, and fundamental questions on the selenolate-capped Au_{25} clusters await to resolve: (1) Whether the $Au_{25}(SeR)_{18}$ nanocluster has the identical geometric structure to that of the $Au_{25}(SR)_{18}$ counterpart? (2) How do the ligands affect the optical and chemical properties of these nanoclusters? These questions are important for understanding the properties of ligand-protected gold nanoclusters.

In this work, through intense efforts we have obtained the crystal structure of $[Au_{25}(SePh)_{18}]^-TOA^+$ which was determined by

X-ray crystallography. Compared to the previously reported $Au_{25}(SCH_2CH_2Ph)_{18}^-$, the $Au_{25}(SePh)_{18}^-$ cluster shows some interesting structural differences, albeit both possess the same icosahedral Au_{13} core and semi-ring $Au_2(SeR)_3$ or $Au_2(SR)_3$ motifs. The photoluminescence, electrochemical properties and the catalytic performance of the $Au_{25}(SePh)_{18}^-$ cluster are also investigated. Time-dependent density functional theory (TD-DFT) analysis is further performed to gain insight into how the ligand affect the electronic structure and the optical absorption spectrum of the $Au_{25}(SePh)_{18}^-$ cluster.

2. Experimental

2.1 Chemicals

All reagents and solvents were commercially available and used as received without further purification, including selenophenol (PhSeH, ≥99.9%), tetrachloroauric(III) acid ($HAuCl_4 \cdot 3H_2O$, ≥99.99% metals basis), tetraoctylammonium bromide (TOAB, ≥98%), sodium borohydride (≥98%), toluene (HPLC, ≥99.9%), methylene chloride (HPLC, ≥99.9%), methanol (HPLC, ≥99.9%). methyl cyanide (HPLC, ≥99.9%), trans-2-[3-(4-tert-butylphenyl)-2-methyl-2-propenylidene]malononitrile (DCTB, ≥98%) and 1,2-diphenethyldiselane (≥98%).

2.2 Synthesis and crystallization of $[Au_{25}(SePh)_{18}]^-TOA^+$ nanoclusters.

The $[Au_{25}(SePh)_{18}]^-TOA^+$ nanoclusters with molecular purity were prepared following a synthetic method reported recently.[34] Briefly, $HAuCl_4 \cdot 3H_2O$ (79.12 mg) was dissolved in 1 mL nanopure water, then phase transferred to toluene with the aid of tetraoctylammonium bromide. After that, the toluene solution of Au (III) was cooled to 0 ^oC in an ice bath over ~30 min without stirring. Then, both C_6H_5SeH (63 µL, dissolved in 1 mL ice-cold toluene) and $NaBH_4$ (11.34 mg, dissolved in 1 mL ice-cold nanopure water) were dropwise added simultaneously to convert Au(III) to nanoclusters. After reaction overnight, the aqueous phase was removed. The mixture in the organic phase was rotavaporated, and then washed several times with CH_3OH to remove the redundant PhSeH and by-products. Finally, pure Au_{25} nanoclusters were obtained through extraction using acetonitrile.

The Au_{25} nanoclusters were crystallized in CH_2Cl_2/ethanol at room temperature (2-3 days), similar to our recent work of $Au_{24}(SePh)_{20}$.[35] Dark crystals were collected, and the structure of $[Au_{25}(SePh)_{18}]^-TOA^+$ was determined by X-ray crystallography.

2.3 Synthesis of $Au_{25}(SeCH_2CH_2Ph)_{18}$ nanoclusters.

For the cluster synthesis, 15 mL of a methanol solution of TOAB (0.131g) was added to 0.5 mL of an aqueous solution of $HAuCl_4 \cdot 3H_2O$ (79.12 mg). After vigorous stirring at room temperature for 30 min, 6 mL of an ethanol solution of $NaBH_4$ (37.8 mg) and 1 mL of an ethanol solution containing $(PhC_2H_4Se)_2$ (50 µL) were rapidly added to the solution. The solution color immediately changed from orange to black. The solution was stirred for 24h. The product was centrifuged at 6500 rpm to remove byproducts such as $(PhC_2H_4Se)_2$ and TOAB. The nanoclusters were extracted from the dried product using acetonitrile.

2.4 X-ray crystallographic determination of $[Au_{25}(SePh)_{18}]^-TOA^+$ nanoclusters.

Single crystal X-ray diffraction data of $[Au_{25}(SePh)_{18}]^-$ was collected on a Bruker Smart 1000 CCD area detector using graphite-monochromatized Mo Kα radiation (λ = 0.71069 Å). A piece of black rhombus-shaped crystal was mounted onto a MiTeGen capillary with fluorolube. Data collection was performed under room temperature (293(2) K) and the structure was solved by direct methods using SHELXS-97.

The structure was solved by direct methods using Bruker program SHELXTL which located all the Au and Se atoms. The remaining non-hydrogen atoms were generated via subsequent difference Fourier syntheses. Most of the selenophenol molecules were fixed as a rigid model adapted from Cambridge Database. After the final refinement, there is still some relatively high residual electron density and solvent accessible voids in structure reported by checkcif outcome, which reveals that solvent molecules are probably present in the structure, but we are unable to locate the solvent molecules in the difference Fourier map. Partial atoms of the tetraoctylammonium cation were found to coexist with the Au_{25} cluster with the help of SQUEEZE routine of PLATON software. However, several tail carbon atoms could not be located due to severe disorder and weak X-ray diffraction. Furthermore, one of the ligands (SeC_6H_5) is disordered over two sets of sites with an occupancy ratio of 0.547 (8):0.453 (8), which was labeled as Se(9), C(49), C(50), C(51), C(52), C(53), C(54) and Se(9'), C(49'), C(50'), C(51'), C(52'), C(53'), C(54'), respectively. All the refinement parameters are summarized in Table S1.

2.5 DFT Calculations

To correlate the cluster structure and optical properties, we carried out time-dependent density functional theory (TDDFT) calculations on the electronic structure and optical absorption spectrum of $Au_{25}(SePh)_{18}^-$. The single crystal structure derived from the XRD analysis was optimized first using Perdew-Burke-Ernzerhof (PBE) functional[38] and then single-point energy calculations with the LB94 functional were performed to obtain the Kohn-Sham (KS) orbital energies and populations. The triple-zeta polarized (TZP) basis set with inclusion of scalar relativistic effect via zeroth-order regular approximation (ZORA) was adopted in all calculations. The TDDFT calculations of excitation energies were also performed using the LB94 functional, which was found to give a good description of excitation curves of thiolate-protected gold clusters.[39,40]

2.6 Characterization

Nuclear magnetic resonance (NMR) analysis was performed on a Bruker Avance spectrometer operating at 400 MHz for 1H and 100MHz for ^{13}C. Deuterated methylene chloride was used as the solvent to dissolve ~10 mg clusters, the residual solvent peaks (i.e. ^1H at 5.32 ppm and ^{13}C at 54.00 ppm) were used as references.

Matrix assisted laser desorption ionization mass spectrometry (MALDI-MS) was performed on an Applied Biosystems Voyager DE-STR MALDI-TOF equipped with a nitrogen laser (337 nm). The mass spectra of negative ions were collected in the linear mode under an acceleration voltage of 25 kV and a delay time of 350 ns. Trans-2-[3-(4-tert-butyl-phenyl)-2-methyl-2-propenylidene] malononitrile (DCTB) was used as MALDI matrix.

UV-vis spectroscopic studies were carried out with an Agilent 8453 diode array spectrometer. Photoluminescence spectra were measured on a FLUOROLOG-3-TAU spectrometer. For the convenience of comparison, the optical density (OD) of all solutions is ~0.05. In these experiments, the particle solutions were prepared in CH_2Cl_2 at a concentration of less than 1 mg·mL^{-1}.

Electrochemical measurements of clusters were performed with an electrochemical workstation (CHI 700E) using a Pt working electrode (diameter 0.4 mm), a Pt wire counter electrode, and a Ag wire quasi-reference electrode in 0.1 M Bu_4NPF_6/CH_2Cl_2. Prior to use, the working electrode was polished with 0.05 mg·mL^{-1} Al_2O_3 slurries and then cleaned by sonication in dilute CH_3CH_2OH and nanopure water successively. The electrolyte solution was deaerated with ultrahigh-purity nitrogen for 40 min and blanketed with a nitrogen atmosphere during the entire experimental procedure.

2.7 Catalytic reduction of 4-nitrophenol using $Au_{25}(SePh)_{18}$ clusters.

The reduction of 4-nitophenol was studied using UV-Vis spectroscopy. The reaction was done under a N_2 atmosphere. In a typical catalytic reaction, nitrophenol (7.0 mg) was dissolved in a 25/5 mL mixture of THF/water. To this solution, $Au_{25}(SePh)_{18}$ nanoclusters were added and the solution was stirred under N_2 atmosphere. After stirring, $NaBH_3CN$ (600 equiv per nitrophenol) in ice cold water was added. Upon addition of $NaBH_3CN$, UV-Vis spectra were recorded.

3. Results and discussion

3.1 Crystal structure of the $Au_{25}(SePh)_{18}^-$ cluster

We previously reported the synthesis of $Au_{25}(SePh)_{18}$ but crystallization was not successful then. Through extensive optimization of crystallization conditions, we have now finally attained the crystal structure. X-ray crystallography shows that the structure of selenophenol-capped Au_{25} cluster indeed resembles that of $Au_{25}(SC_2H_4Ph)_{18}^-$.[21,22] For comparison, both crystal structures are displayed in Figure 1. The $Au_{25}(SePh)_{18}^-$ contains a centered icosahedral Au_{13} core, which is capped by an exterior shell composed of six $Au_2(SePh)_3$ motifs (Figure 1A). The Au_{13} core possesses three mutually perpendicular 2-fold axes (x, y and z, Figure 1C). Similar to the $Au_{25}(SC_2H_4Ph)_{18}^-$ (Figure 1B), the selenium atoms bent out of the atomic plane defined by the σ_h symmetry plane (D_{2h} sublet of an icosahedron). For instance, if one views along the σ_h plane in x-y (Figure 1A), one of the Se atoms in the Se-Au-Se-Au-Se motif is bent downward, while the inverse Se atom is bent upward. Similar distortions are also observed in the σ_h planes along y-z and x-z.

Despite the close resemblance of $Au_{25}(SePh)_{18}^-$ to $Au_{25}(SC_2H_4Ph)_{18}^-$, there are some structural differences between the two clusters worthy of commenting. Comparing with the Au_2S_3 in the σ_h plane along x-y (Figure 1E), the distortion of the Se atoms in the Au_2Se_3 within the σ_h plane is more obvious (Figure 1D), and so is it in the x-z plane. However, in the σ_h plane along y-z, the six Se atoms are nearly on the same plane (the sum of angles of hexagon is 717.24°), which is different from that of $Au_{25}(SC_2H_4Ph)_{18}^-$ (Figure S2). On the other hand, the average bond length of Au-Se bond (2.434 Å) in the 'V-shaped' semi-ring Se-Au-Se-Au-Se motifs is much longer than the Au-S bond in $Au_{25}(SC_2H_4Ph)_{18}^-$ (average 2.301 Å), which is due to the larger covalent radius of Se atom (covalent radius of selenium r =1.20 Å vs. sulfur atom r =1.05 Å). But the angle of Au-Se-Au in the Au_2Se_3 motif (average 94.89°) is much smaller than the Au-S-Au in $Au_{25}(SC_2H_4Ph)_{18}^-$ (average 102.677°). In addition, the overall diameter of the $Au_{25}Se_{18}$ framework, which was defined as the distance between two outermost Se atoms (12.074 Å, 12.238 Å and 12.403 Å along z, x, and y directions, respectively), is also larger than the values of $Au_{25}S_{18}$ (11.995 Å, 12.016 Å and 12.061 Å, respectively). Besides the increase in the diameter of the overall $Au_{25}Se_{18}$ framework, we found that the radial Au-Au distance in the Au_{13}-icosahedron was also slightly increased upon the replacement of thiolate ligand by selenolate (i.e. average 2.797±0.01 Å in the $Au_{25}(SePh)_{18}^-$ versus 2.775±0.01 Å of $Au_{25}(SC_2H_4Ph)_{18}^-$). Hence, not only the exterior ligand shell but also the Au_{13} core become more expanded induced by the ligand change from thiolate to selenolate, which should also affect the distribution of the electron density and molecular orbital energies of the cluster.

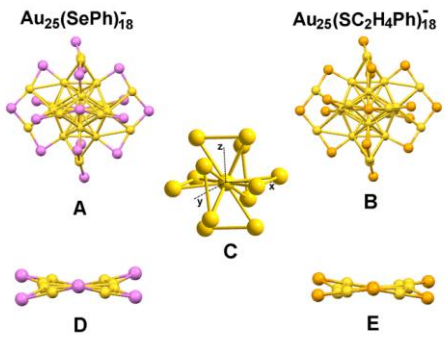

Figure 1. Comparison of the crystal structures of $Au_{25}(SePh)_{18}^-$ (A) and $Au_{25}(SC_2H_4Ph)_{18}^-$ (B) clusters; (C) The Au_{13} core of the $Au_{25}(SePh)_{18}^-$; Comparison of the distortions of the Au_2Se_3 (D) and Au_2S_3 motifs (E) in the σ_h plane along x-y (Color labels: yellow = Au, violet = Se, orange = S, for clarity C and H atoms are omitted).

3.2 Confirmation of the $[Au_{25}(SePh)_{18}]^-TOA^+$ formula by NMR and Mass Spectrometry Analyses

In the X-ray single crystal structural analysis, the $[CH_3(CH_2)_6CH_2]_4N^+$ counterion (abbreviated TOA^+) for the anionic

cluster was found, albeit the carbon chains were heavily disordered (Figure S1). To confirm this, we performed nuclear magnetic resonance (NMR). As shown in Figure 2A, the peaks at 6-8 ppm (90 H) are assigned to -C_6H_5, the peaks at 2.90 ppm (7.87 H, labelled as **a**) to the -CH_2- directly connected to the N atom in TOA^+), the 1.48 and 1.24 ppm peaks (labelled as **b** and **c**) to the methylene chain of TOA^+ , and the peak at 0.85 ppm (12.20 H, labelled as **d**) to the -CH_3 group. According to the proton ratio ((-$SeC_6H_5)_{18}$: (-N-CH_2-)$_4$: (-CH_3)$_4$ = 90 : 7.87 : 12.20), we determined the ratio of $[Au_{25}(SePh)_{18}]^-$ to TOA^+ is 1:1. ^{13}C-NMR analysis (Figure 2B) show peaks in the range of 0-30 ppm from the TOA^+ group and the peak at ~130 ppm from the PhSe group (note: the intense 54.0 ppm peak is the solvent residual signal).

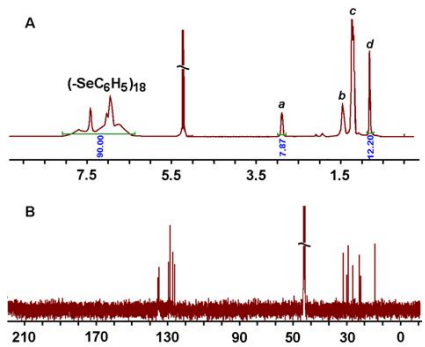

Figure 2. ^{1}H NMR (A) and ^{13}C NMR (B) spectra of $[Au_{25}(SePh)_{18}]^-TOA^+$ cluster (single crystal redissolved in CD_2Cl_2).

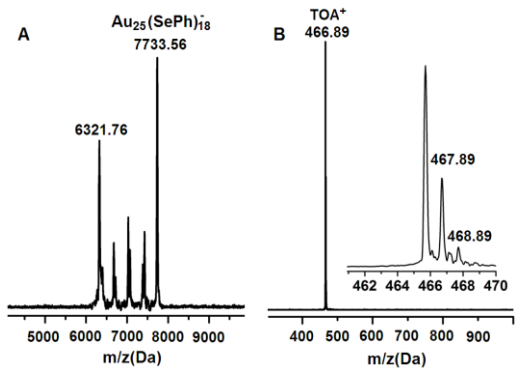

Figure 3. MALDI-MS analysis of $[Au_{25}(SePh)_{18}]^-TOA^+$. (A) Negative mode mass spectrum of $[Au_{25}(SePh)_{18}]^-$. (B) Positive mode spectrum for the counterion $[TOA]^+$, where TOA^+ = $(C_8H_{17})_4N^+$ (single crystal redissolved in CH_2Cl_2).

We further performed the MALDI-MS to confirm the existence of the TOA^+. MALDI-MS revealed a prominent peak at m/z= 7733.56 (Figure 3A), which is assigned to $[Au_{25}(SePh)_{18}]^-$ (cal. 7734.39 Da), and the other peaks are its fragments. As shown in Figure 3B, a prominent peak at 466.89 Da was observed in the low m/z range at positive mode, which is assigned to TOA^+ (cal. 466.53 Da). All these results show that the precise formula of the cluster is $[Au_{25}(SePh)_{18}]^-TOA^+$, which is consistent with the X-ray crystallographic analysis.

3.3 Electrochemical Properties of the $Au_{25}(SePh)_{18}^-$ cluster.

To investigate the electrochemical properties of $Au_{25}(SePh)_{18}$ nanocluster, we performed square wave voltammograms (SWVs) of $Au_{25}(SePh)_{18}$ and $Au_{25}(SCH_2CH_2Ph)_{18}$ nanoclusters at room temperature in 0.1 M Bu_4NPF_6/CH_2Cl_2 (Figure 4). Four oxidation peaks are found at 0.05 (O1), 0.75 (O2), 0.95 (O3) and 1.37 V (O4) versus Ag/Ag^+ of the $Au_{25}(SePh)_{18}$, as well as four reduction peaks at -1.19 (R1), -1.61 (R2), -1.77 (R3) and -2.02V (R4) (Figure 4A). But, there are only two reduction peaks in the SWV of $Au_{25}(SCH_2CH_2Ph)_{18}$ nanoclusters (Figure 4B). Of note, the O_2 peak (indicated by *) is very close to the R1 peak and Figure S3 shows the changing currents for different residual-oxygen contents, which clearly confirms that it is from O_2.

According to the SWV of $Au_{25}(SePh)_{18}$ nanoclusters, we determined the electrochemical HOMO−LUMO energy gap of the $Au_{25}(SePh)_{18}$ to be only ~1.24 V (i.e. the difference between O1 and R1, Figure 4A), which is substantially smaller than that of the phenylethylthiolate-protected Au_{25} (~1.62 V, Figure 4B). Lee group has reported that the O1−O2 gap was critically dependent upon the change in the dielectric environment surrounding the gold core.[41] In the $Au_{25}(SePh)_{18}$ nanoclusters, the O1−O2 gap (~0.70 V) is significantly different from that of $Au_{25}(SC_2H_4Ph)_{18}$ nanoclusters (~0.30V), indicating the dielectric environment provided by the selenophenol ligand is quite different than the phenylethanethiol. Moreover, in the $Au_{25}(SePh)_{18}$ nanoclusters, the O2 peak is much smaller than the O1 peak, indicating the first oxidation state (O1) is more stable than the second oxidation state (O2). But, in the $Au_{25}(SC_2H_4Ph)_{18}$ nanoclusters, the O2 peak is close to the O1 peak (the gap of O1-O2 is ~0.30 V), indicating that both $Au_{25}(SC_2H_4Ph)_{18}^0$ and $Au_{25}(SC_2H_4Ph)_{18}^-$ can mutual transformation, which has been proved by Zhu et al.[42]

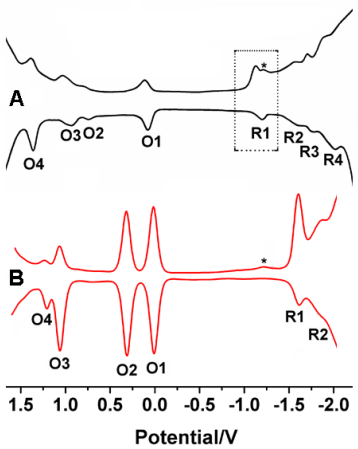

Figure 4. Square-wave voltammograms (SWVs) of $Au_{25}(SePh)_{18}$ (A) and $Au_{25}(SCH_2CH_2Ph)_{18}$ (B) nanoclusters in CH_2Cl_2 containing 0.1M Bu_4NPF_6. The concentration of clusters was 3 mg/mL. (The * indicates wave for incompletely removed O_2).

3.4 Catalytic performance of the $Au_{25}(SePh)_{18}$ nanocluster

In order to further study the $Au_{25}(SePh)_{18}$ nanocluster, we also investigated its catalytic performance. In previous work, the $Au_{25}(SR)_{18}$ nanocluster has been extensively investigated in a range of reactions, most of which are catalytic oxidation and reduction processes,[43-47] such as the oxidation of CO and benzoic alcohol, selective reduction of benzylidene acetone and α,β-unsaturated ketone. Recently Scott et al explored the catalytic activity of $Au_{25}(SR)_{18}$ nanoclusters for the reduction of *4*-nitrophenol and unraveled the robust nanoclusters remained intact after catalytic circles. The results demonstrated that the nanocluster catalysts were recyclable. Herein, the selective reduction of *4*-nitrophenol is chosen to test the activity of the newly obtained $Au_{25}(SePh)_{18}$ nanoclusters.

In this process, we also performed the entire reaction under N_2 atmosphere, but the only difference is that we used the $NaBH_3CN$ instead of the $NaBH_4$. As shown in the Figure 5, before adding the $Au_{25}(SePh)_{18}$ nanoclusters, the absorbance of the *4*-nitrophenolate ion is at 400 nm; after adding the $Au_{25}(SePh)_{18}$ nanoclusters, a new band is also seen at 312 nm due to the formation of *4*-aminophenol product, indicating that the $Au_{25}(SePh)_{18}$ nanoclusters catalyzed the reaction. And the rate constant of the $Au_{25}(SePh)_{18}$-catalysed reduction of *4*-nitrophenol is 0.12±0.02 min^{-1}.

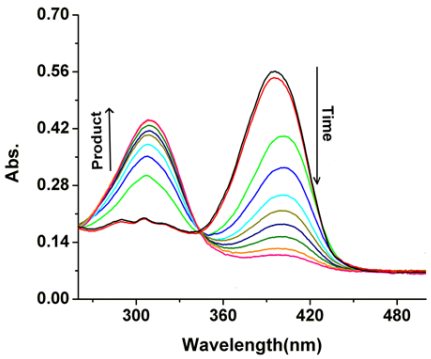

Figure 5. Representative UV-Vis spectra of the reduction of 4-nitrophenolate to 4-aminophenol over $Au_{25}(SePh)_{18}$ nanoclusters.

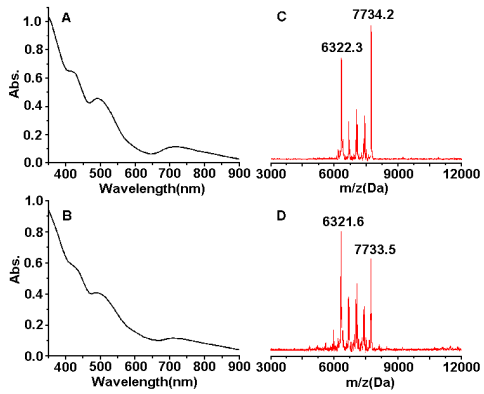

Figure 6. (A) UV-Vis spectra of $Au_{25}(SePh)_{18}$ nanoclusters before and (B) after catalysis, (C) MALDI mass spectra of $Au_{25}(SePh)_{18}$ clusters before and (D) after catalysis (the peak at 7734.2 or 7733.5 Da is assign to the $Au_{25}(SePh)_{18}$ (cal. 7734.39 Da), and the other peaks are its fragments, which are not impurities because single crystal $Au_{25}(SePh)_{18}$ samples also give rise to identical fragments.).

In order to study whether the $Au_{25}(SePh)_{18}$ nanoclusters remained stable or not in the process, we isolated the nanoclusters after catalysis and re-characterized with UV-Vis and MALDI-MS. As shown in the Figure 6, UV-Vis and MALDI-MS data clearly indicate the integrity of the $Au_{25}(SePh)_{18}$ nanoclusters after the catalytic process. These results indicate that the $Au_{25}(SePh)_{18}$ nanoclusters are sufficiently robust and also have potential application in catalysis.

3.5 TD-DFT analysis of the electronic structure of the $Au_{25}(SePh)_{18}$ cluster

To correlate the cluster structure and optical properties, we have performed time-dependent density functional theory (TD-DFT) calculations for the electronic structure and optical absorption spectrum of $Au_{25}(SePh)_{18}^-$. In order to better compared with the experimental results, we used the -SePh as ligands to calculate the electronic structure and optical absorption spectrum of $Au_{25}(SePh)_{18}^-$ in the TD-DFT calculations (Figure S4). The calculated optical absorption spectrum, Kohn-Sham molecular orbitals (MO), energies, and atomic orbital (AO) contributions are displayed in Figure 7. As shown in Figure 7A, the theoretical spectrum for $Au_{25}(SePh)_{18}^-$ shows three feature peaks centered at 430 nm (peak ***c***), 620 nm (peak ***b***) and 1050 nm (peak ***a***). In comparison to the experimental results, the theoretical results underestimate the optical gap. The theoretical prediction is 1.06 eV, which is lower than the experimental result 1.24 eV.[32] On the other hand, the first feature absorption peak is predicted to locate at 1050 nm, which is red-shift about 300 nm in comparison to the experimental result. The large errors of theoretical predictions of the location of first absorption peak (***a***) might be caused by the exchange-correlation functional. In present, we have evaluated PBE, LDA (X-alpha) and LB94 functionals, which all give rise to the similar shape of optical curves. Thus, the primary features (i.e. the three major absorption peaks ***a-c***) are reasonably reproduced in the TDDFT calculations.

Further examination of the Kohn-Sham (KS) molecular orbital (MO) energy levels and atomic orbital components in each KS MO of $Au_{25}(SePh)_{18}^-$ indicates that the icosahedral Au_{13}-core contributes mainly to the two strong absorption peaks (***a*** and ***b***) in the optical spectrum. Figure 7B represents the KS orbital energies and components of $Au_{25}(SePh)_{18}^-$. As shown in Figure 7B, the set of frontier orbitals including occupied orbitals HOMO-2 to HOMO and unoccupied LUMO to LUMO+7 are mainly composed of the Au(6sp) atomic orbital, denoted as the *sp*-band. The occupied orbitals below HOMO-2 are *d*-band due to significant contribution of Au(5d) atomic orbital. From Figure 7B, the first excited state occurs at 1.30 eV (peak ***a***) and corresponds to a HOMO to LUMO transition, which is essentially an intraband (*sp* to *sp*) transition. The other two high-energy feature absorption peaks involve interband transitions (e.g. *sp* → *sp* and *d* → *sp*) transition.

It is of interest to compare the optical curves and electronic structures between $Au_{25}(SePh)_{18}^-$ and the previous reported $Au_{25}(SC_2H_4Ph)_{18}^-$ as they have very similar atomic frameworks and icosahedral Au_{13}-core. The computed excitation energy curve of $Au_{25}(SC_2H_4Ph)_{18}^-$ is displayed in Figure 7C. It is found that the optical gap of $Au_{25}(SePh)_{18}^-$ is smaller than the $Au_{25}(SC_2H_4Ph)_{18}^-$ and the first strong absorption peak of $Au_{25}(SePh)_{18}^-$ is red-shifted in comparison to $Au_{25}(SC_2H_4Ph)_{18}^-$. These tendencies are in good agreement with experiment.[32] To find out the electronic structure difference between two clusters, we have computed the KS orbital energies and components of $Au_{25}(SC_2H_4Ph)_{18}^-$ as well (Figure 7C). From Figure 7B and Figure 7C, the HOMO and LUMO energies of $Au_{25}(SePh)_{18}^-$ are -7.37 and -6.31 eV, respectively, which are both more negative than those of $Au_{25}(SC_2H_4Ph)_{18}^-$ (the calculated HOMO and LUMO energies are -7.11 and -5.88 eV, respectively). Moreover, the HOMO-LUMO gap of $Au_{25}(SPh)_{18}^-$ is 1.138 eV compulated by Aikens.[48] This kind of change rule is consistent with the experimental results (the HOMO-LUMO gap of $Au_{25}(SC_2H_4Ph)_{18}^-$, $Au_{25}(SPh)_{18}^-$ and $Au_{25}(SePh)_{18}^-$ are 1.33eV, 1.29eV and 1.24eV, respectively.[49]).

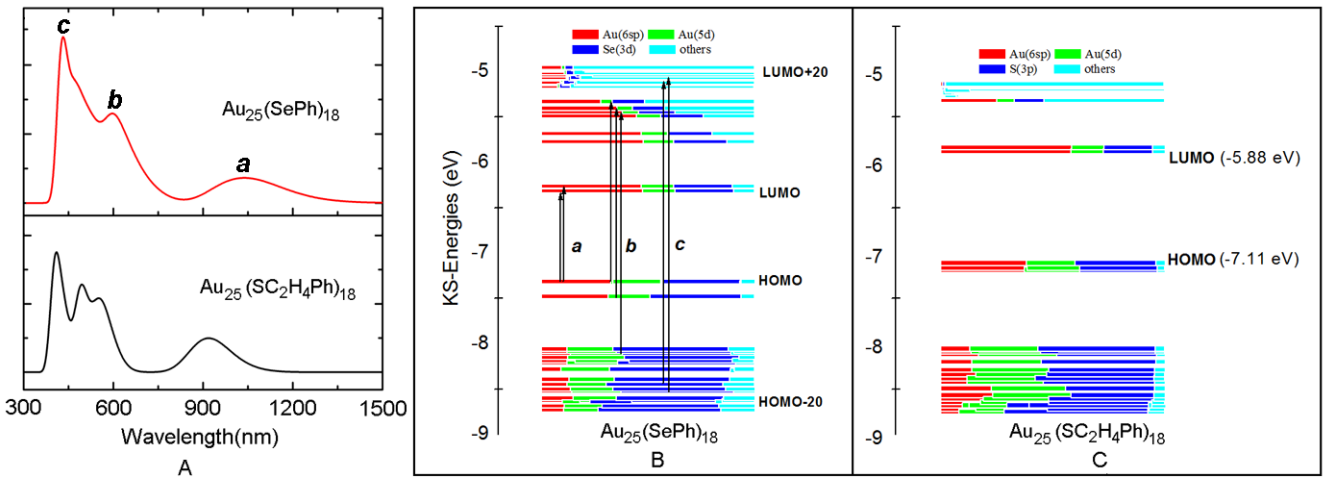

Figure 7. (A) Comparison of theoretical optical curve of $Au_{25}(SePh)_{18}$ and $Au_{25}(SC_2H_4Ph)_{18}$ nanocluster. Comparison of the component of KS orbitals of $Au_{25}(SePh)_{18}$ (B) and $Au_{25}(SC_2H_4Ph)_{18}$ (C) nanocluster.

As shown in Figure 7B and Figure 7C, the Au(6sp) contributions in HOMO and LUMO are both decreased along with the replacement of thiolate by selenolate (37.82% and 57.57% in $Au_{25}(SC_2H_4Ph)_{18}^-$ and 33.39% and 47.18% in $Au_{25}(SePh)_{18}^-$). For comparison, the Au(5d) contributions in HOMO and LUMO are both nearly unchanged upon the ligand replacement. However, an increase of the atomic orbital contribution from the hydrocarbons (C and H atoms) in HOMO and LUMO is clearly found for $Au_{25}(SePh)_{18}^-$. In $Au_{25}(SePh)_{18}^-$, the PhSe-ligand has two carbon-atoms shorter than the PhC_2H_4S-ligand in $Au_{25}(SC_2H_4Ph)_{18}^-$, which could induce stronger interactions between the Au-core and phenyl rings and thereby increase the contribution of atomic orbitals of hydrocarbon groups to the HOMO and LUMO. Recently, Zhu et al. shown that a surprising 2.5 times photoluminescence enhancement for the $PhCH_2S$-capped Au_{24} and Au_{20} nanoclusters comparing to the PhC_2H_4S-capped analogues,[50] indicated that the interactions between phenyl rings in ligand shell and Au-core played important role on affecting the electronic structure and optical properties of the cluster. On the other hand, the charge populations of $Au_{25}(SePh)_{18}^-$ and $Au_{25}(SC_2H_4Ph)_{18}^-$ are examined using Hirshfeld charge analysis method. The Au-core in the $Au_{25}(SePh)_{18}^-$ and $Au_{25}(SC_2H_4Ph)_{18}^-$ carries -0.1|e| and -0.27|e|, respectively, indicating the selenolate ligand modifies the interface charge transfers between the Au-core and ligand shells, which is correlated with the experimental discovery of expanded Au-core by selenolate capping.

3.6 Optical Properties of the $Au_{25}(SePh)_{18}^-$ cluster.

We also compared the fluorescence spectra of $Au_{25}(SePh)_{18}$ and $Au_{25}(SC_2H_4Ph)_{18}$ nanoclusters (Figure 8). The $Au_{25}(SePh)_{18}$ clusters exhibit feeble photoluminescence with its peak at ~1100 nm, and is significantly weaker than that of $Au_{25}(SC_2H_4Ph)_{18}$ clusters. The observation here is reasonable, as the ligand effect on the fluorescence intensity was reported previously by Jin and co-worker.[51] They found that the fluorescence intensities of three

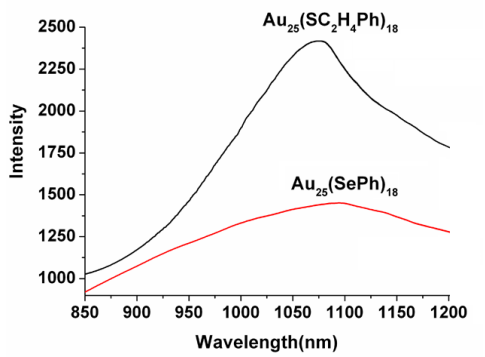

Figure 8. The fluorescence spectra of $Au_{25}(SCH_2CH_2Ph)_{18}$ and $Au_{25}(SePh)_{18}$ nanoclusters. The emission spectra were acquired at λ_{ex}=447 nm and λ_{ex}=430 nm, respectively.

species of $[Au_{25}(SR)_{18}]^-$ (R= $-SC_2H_4Ph$, $-SC_{12}H_{25}$, $-SC_6H_{13}$) were largely enhanced by charge transfer from the surface ligands to the metal core. In our work, changing the ligand of thiolate to selenolate weakens the fluorescence intensity and the reason should be that the charge transfer across the Se-Au bond is less pronounced than across the S-Au. Meanwhile, the fluorescence spectrum of $Au_{25}(SePh)_{18}$ shows a 25-nm red-shift compared to that of $Au_{25}(SC_2H_4Ph)_{18}$, which is in line with the redshift of the UV-vis absorption peaks. These results demonstrate that the surface ligands play a considerable role in the fluorescent property of nanoclusters.

In order to further understand how the ligand affects the optical properties, we prepared the $Au_{25}(SeC_2H_4Ph)_{18}$ nanocluster. The $Au_{25}(SeCH_2CH_2Ph)_{18}$ nanoclusters are characterized by MALDI-MS and UV-vis (Figure 9). In the MALDI-MS spectrum, the peak at 8236.4 Da is assigned to the molecular ion peak of $Au_{25}(SeCH_2CH_2Ph)_{18}$ (cal. 8238.95 Da). It is worth noting that the fragmentation of $Au_{25}(SeCH_2CH_2Ph)_{18}$ is less than that of $Au_{25}(SePh)_{18}$.

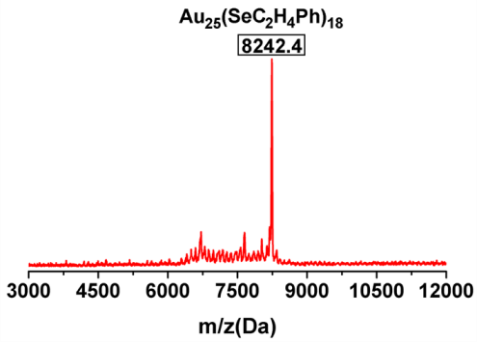

Figure 9. MALDI-MS spectrum of the $Au_{25}(SeCH_2CH_2Ph)_{18}$ nanoclusters.

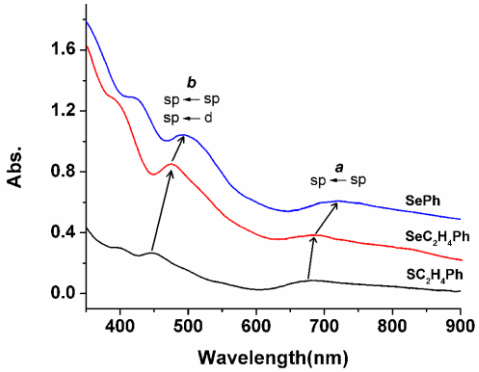

Figure 10. Comparison of the UV-vis absorption spectra of $Au_{25}(SC_2H_4Ph)_{18}$, $Au_{25}(SeC_2H_4Ph)_{18}$ and $Au_{25}(SePh)_{18}$ nanoclusters. The spectra are vertically shifted for comparison.

The UV-vis spectrum of the $Au_{25}(SeCH_2CH_2Ph)_{18}$ nanoclusters show absorption peaks at 400, 470 and 683 nm (Figure 10), which are consistent with the case of $Au_{25}(SeC_8H_{17})_{18}$ nanoclusters reported by Negishi.[29] By compaing the spectra of $Au_{25}(SeC_2H_4Ph)_{18}$ and $Au_{25}(SC_2H_4PH)_{18}$ —which bears no conjugation within the carbon tails, one can see a ~20 nm for the **b** band and ~8 nm for the **a** band (Figure 10), thus the change of S to Se atom at the gold-ligand interface somewhat affects the energy level positions and optical absorption peaks. Further comparison between $Au_{25}(SeC_2H_4Ph)_{18}$, and $Au_{25}(SePh)_{18}^-$ identifies the conjugation effect in the ligand, and such an effect gives rise to an obvious redshift of all the absorption peaks from to 400, 470 and 683 nm to 430, 500 and 725 nm, respectively, that, 30-50 nm redshift; thus, the ligand conjugation effect is more important than the S/Se effect. Taken together, both the chalcogenide atom (S, Se) and hydrocarbon group (R: $-C_8H_{17}$, $PhCH_2CH_2$-, Ph-) make contributions to the optical absorption of gold nanoclusters.

Conclusions

In summary, we have successfully crystallized the selenolate-capped Au_{25} nanocluster and the solved crystal structure provides a firm basis for understanding the differences of electronic structure, Au-S/Se interfacial bonding, and optical properties between $Au_{25}(SePh)_{18}^-$ and its thiolate counterpart. The $Au_{25}(SePh)_{18}^-$ exhibits a similar structure to the previously reported $Au_{25}(SCH_2CH_2Ph)_{18}^-$ nanocluster.[20,21] However, the electronic structure and properties of Au_{25} cluster are strongly affected by the ligand change. The replacement of thiolate ligand by selenolate renders redshift of absorption peaks of Au_{25} cluster and more negative HOMO and LUMO energy levels, hence, stablization of the cluster. The determination of the atomic structure of selenolate-capped Au_{25} nanoclusters opens up the door for further exploring the optical and photocatalytic properties of selenolate-protected Au nanoclusters and for comparison with the well-established thiol-protected counterparts.

Acknowledgements

We acknowledge financial support by NSFC (21072001, 21201005, 21372006), the Ministry of Education and Ministry of Human Resources and Social Security, the Education Department of Anhui Province, Anhui Province International Scientific and Technological Cooperation Project, 211 Project of Anhui University. YP acknowledge financial support by NSFC (21103144, 21373176), Hunan Provincial Natural Science Foundation of China (12JJ7002, 12JJ1003) and Scientific Research Fund of Hunan Provincial Education Department (13A100).

Notes and references

[a]Department of Chemistry and Center for Atomic Engineering of Energy Meterials, Anhui University.

[b]Department of Chemistry, Key Laboratory of Environmentally Friendly Chemistry and Applications of Ministry of Education, Xiangtan University, Hunan Province 411105, P. R. China.

*Email: ypnku78@gmail.com (theory); zmz@ahu.edu.cn (experiment)

Electronic Supplementary Information (ESI) available: [details of any supplementary information available should be included here]. See DOI: 10.1039/b000000x/

1 H. Qian, M. Zhu, Z. Wu and R. Jin, *Acc. Chem. Res.* 2012, **45**, 1470-1479.
2 J. Nishigaki, R. Tsunoyama, H. Tsunoyama, N. Ichikuni, S. Yamazoe, Y. Negishi, M. Ito, T. Matsuo, K. Tamao and T. Tsukuda, *J. Am. Chem. Soc.* 2012, **134**, 14295-14297.
3 A. Tlahuice-Flores, M. Jose-Yacaman and R. Whetten, *Phys. Chem. Chem. Phys.* 2013, **15**, 19557-19560.
4 E. S. Shibu and T. Pradeep, *Chem. Mater.* 2011, **23**, 989-999.
5 A. Dass, *J. Am. Chem. Soc.* 2011, **133**, 19259-19261.
6 S. Knoppe, R. Azoulay, A. Dass and T. Bürgi, *J. Am. Chem. Soc.* 2012, **134**, 20302-20305.
7 H. Yao, *J. Phys. Chem. Lett.* 2012, **3**, 1701-1706.
8 R. Wyrwas, M. Alvarez, J. Khoury, R. Price, T. Schaaff and R. Whetten, *Eur. Phys. J. D.* 2007, **43**, 91-95.
9 N. de Silva and L. Dahl, *Inorg. Chem.* 2005, **44**, 9604-9606.
10 Y. Shichibu, Y. Kamei and K. Konishi, *Chem. Commun.* 2012, **48**, 7559-7561.
11 X. Wan, Z. Lin and Q. Wang, *J. Am. Chem. Soc.* 2012, **134**, 14750-14752.
12 A. Das, T. Li, K. Nobusada, Q. Zeng, N. L. Rosi and R. Jin, *J. Am. Chem. Soc.* 2012, **134**, 20286-20289.
13 H. Yang, Y. Wang, J. Lei, L. Shi, X. Wu, V. Mäkinen, S. Lin, Z. Tang, J. He, H. Häkkinen, L. Zheng and N. Zheng, *J. Am. Chem. Soc.* 2013, **135**, 9568-9571.
14 N. Zheng and G. Stucky, *J. Am. Chem. Soc.* 2006, **128**, 14278-14280.
15 H. Fan, K. Yang, D. Boye, T. Sigmon, K. Malloy, H. Xu, G. Lopez and C. Brinker, *Science* 2004, **304**, 567-571.
16 N. Rosi, D. Giljohann, C. Thaxton, A. Lytton-Jean, M. Han and C. Mirkin, *Science* 2006, **312**, 1027-1030.
17 H. Wohltjen, A. W. Snow, *Anal. Chem.* 1998, **70**, 2856-2859.
18 C. Huang, C. Chiang, Z. Lin, K. Lee and H. Chang, *Anal. Chem.* 2008, **80**, 1497-1504.
19 C. Lin, T. Yang, C. Lee, S. Huang, R. Sperling, M. Zanella, J. Li, J. Shen, H. Wang, H. Yeh, W. Parak and W. Chang, *ACS Nano* 2009, **3**, 395-401.
20 Y. Shichibu, Y. Negishi, T. Tsukuda and T. Teranishi, *J. Am. Chem. Soc.* 2005, **127**, 13464-13465.
21 M. Zhu, C. Aikens, F. Hollander, G. Schatz and R. Jin, *J. Am. Chem. Soc.* 2008, **130**, 5883-5885.
22 M. Heaven, A. Dass, P. White, K. Holt and R. Murray, *J. Am. Chem. Soc.* 2008, **130**, 3754-3755.
23 T. Dainese, S. Antonello, J. Gascón, F. Pan, N. Perera, M. Ruzzi, A. Venzo, A. Zoleo, K. Rissanen and F. Maran, *ACS Nano*, 2014, **8**, 3904-3912.
24 Z. Tang, T. Ahuja, S. Wang and G. Wang, *Nanoscale* 2012, **4**, 4119-4124.
25 S. Wang, X. Zhu, T. Cao and M. Zhu, *Nanoscale* 2014, **6**, 5777-5781.
26 H. Chong, P. Li, S. Wang, F. Fu, J. Xiang, M. Zhu and Y. Li, *Sci. Rep.* 2013, **3**, 3214-3217.
27 M. Zhu, C. M. Aikens, M. P. Hendrich, R. Gupta, H. Qian, G. C. Schatz and R. Jin, *J. Am. Chem. Soc.* 2009, **131**, 2490-2492.
28 S. Antonello, N. Perera, M. Ruzzi, J. Gascón and F. Maran, *J. Am. Chem. Soc.* 2013, **135**, 15585-15594.
29 Y. Negishi, W. Kurashige and U. Kamimura, *Langmuir* 2011, **27**, 12289-12292.
30 W. Kurashige, M. Yamaguchi, K. Nobusada and Y. Negishi, *J. Phys. Chem. Lett.* 2012, **3**, 2649-2652.
31 W. Kurashige, S. Yamazoe, K. Kanehira, T. Tsukuda and Y. Negishi, *J. Phys. Chem. Lett.* 2013, **4**, 3181-3185.
32 X. Meng, Q. Xu, S. Wang and M. Zhu, *Nanoscale* 2012, **4**, 4161-4165.
33 Q. Xu, S. Wang, Z. Liu, G. Xu, X. Meng and M. Zhu, *Nanoscale* 2013, **5**, 1176-1182.
34 Y. Song, T. Cao, H. Deng, X. Zhu, P. Li and M. Zhu, *Sci China Chem* doi: 10.1007/s11426-014-5071-5.
35 Y. Song, S. Wang, J. Zhang, X. Kang, S. Chen, P. Li, H. Sheng and M. Zhu, *J. Am. Chem. Soc.* 2014, **136**, 2963-2965.
36 C. Yee, A. Ulman, J. Ruiz, A. Parikh, H. White and M. Rafailovich, *Langmuir* 2003, **19**, 9450-9458.
37 A. Das, T. Li, G. Li, K. Nobusada, C. Zeng, N. Rosi and R. Jin, *Nanoscale* 2014, **6**, 6458-6462.
38 J. P. Perdew, K. Burke and M. Ernzerhof, *Phys. Rev. Lett.* 1996, **77**, 3865-3868.
39 C. M. Aikens, *J. Phys. Chem. A* 2009, **113**, 10811-10817.
40 Y. Pei, S. Lin, J. Su and C. Liu, *J. Am. Chem. Soc.* 2013, **135**, 18067-18079.
41 D. Lee, R. Donkers, G. Wang, A. Harper and R. Murray, *J. Am. Chem. Soc.* 2004, **126**, 6193-6199.
42 M. Zhu, W. Eckenhoff, T. Pintauer and R. Jin, *J. Phys. Chem. C* 2008, **112**, 14221-14224.
43 X. Nie, H. Qian, Q. Ge, H. Xu and R. Jin, *ACS Nano.* 2012, **6**, 6014-6022.
44 S. Xie, H. Tsunoyama, W. Kurashige, Y. Negishi and T. Tsukuda, *ACS Catal.* 2012, **2**, 1519-1523.
45 Y. Zhu, H. Qian, B. Drake and R. Jin, *Angew. Chem. Int. Ed.* 2010, **49**, 1295-1298.

46 A. Shivhare, S. Ambrose, H. Zhang, R. Purves and R Scott, *Chem.Commun.* 2013, **49**, 276-278.
47 H. Yamamoto, H. Yano, H. Kouchi, Y. Obora, R. Arakawa and H. Kawasaki, *Nanosacle* 2012, **4**, 4148-4154.
48 C. M. Aikens, *J. Phys. Chem. Lett.*, 2010, **1**, 2594-2599.
49 R. Guo and R. W. Murray, *J. Am. Chem. Soc.* 2005, **127**, 12140-12143.
50 X. Zhu, S. Jin, S. Wang, X. Meng, C. Zhu, M. Zhu and R. Jin, *Chem. Asian J.* 2013, **8**, 2739-2745.
51 Z. Wu and C. Jin, *Nano Lett.* 2010, **10**, 2568-2573.

The TOC of this manuscript

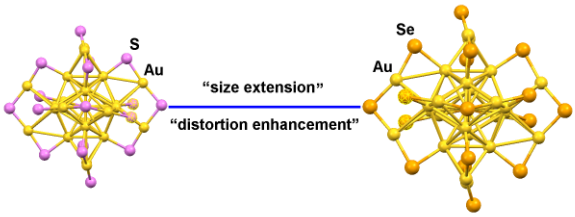

Compared with $Au_{25}(SC_2H_4Ph)_{18}$, the $Au_{25}(SePh)_{18}$ has some worthy-of-mentioning differences in structure and properties.